THE EUROPEAN
PHYSICAL JOURNAL PLUS

Investigation of turbulent flow structures in a wall jet can combustor: application of large eddy simulation

Mohammad Sadegh Abedinejad[1]**, Farzad Bazdidi-Tehrani**[2,a] **, Sajad Mirzaei**[2]

[1] Department of Mechanical Engineering, Faculty of Engineering and Technology, Alzahra University, Tehran, Iran
[2] School of Mechanical Engineering, Iran University of Science and Technology, 16846-13114 Tehran, Iran

Abstract The present paper's main goal is to investigate the turbulence structures and combustion characteristics in a model wall jet can combustor (WJCC) employing the large eddy simulation (LES) approach. The laminar flamelet combustion and discrete ordinates radiation models are applied in an Eulerian–Lagrangian approach to simulate a reactive spray flow. The results illustrate that LES together with an appropriate mesh and a suitable time step could properly capture the coherent vortical structures, including vortex tube, streamwise and hairpin vortices throughout the model WJCC. Also, the energy cascade from the largest turbulence length scale (integral length scale) at lower frequency of the spectrum to the smallest one along with the recirculation zones is revealed suitably. At the beginning of WJCC, immediately after the swirler, a region of dense coherent structures is formed that can influence the sharp fluctuations of the droplet. In the primary and intermediate zones the hairpin vortices and in the dilutions zone the streamwise vortices are observed more. A significant temperature reduction and a maximum scalar dissipation rate are detected in the head of hairpins. Results also indicate that the strain rate and flow temperature have an inverse relationship. The greatest strain rate is visible at the center of the collision of the primary jets and the main stream, where there is minimum temperature. The largest values of temperature are detected in the intermediate zone under the influence of the largest reverse flow.

Abbreviations

A_d	Droplet surface area
B_m	Spalding mass transfer number
B_T	Spalding heat transfer number
C_D	Drag coefficient
c_p	Specific heat capacity (J/kg K)
CFL	Courant (Courant–Friedrichs–Lewy) number
D	Diameter of WJCC
$D_{i,m}$	Diffusion coefficient of vapor in gas phase

[a] e-mail: bazdid@iust.ac.ir (corresponding author)

Springer

d_p	Diameter of droplet
d_{si}	Swirler inside diameter
E_{uu}	Power spectrum density of axial velocity fluctuations
F_i	Body force in momentum equations
f	Mixture fraction
f'	Mixture fraction variance
H	Enthalpy
h	Heat transfer coefficient
h_{fg}	Latent heat of vaporization
k	Turbulence kinetic energy
L	Integral length scale
L_s	Sub-grid length scale
LES	Large eddy simulation
m	Mass (kg)
Nu	Nusselt number
P	Pressure (Pa)
$p(f)$	Probability density function (PDF)
Pr	Prandtl number
PSD	Power spectrum density
Q	Second invariant of velocity gradient tensor
q_ϕ^{sgs}	Sub-grid-scale turbulent fluxes of scalars
RANS	Reynolds-averaged Navier–Stokes
Re	Reynolds number
RMS	Root mean square
RSM	Reynolds stress model
Sc	Schmidt number
sgs	Sub-grid scale
$\dot{S}$	Source term
S_{ij}	Strain rate tensor
Sc_{sgs}	Sub-grid-scale Schmidt number
T	Temperature (K)
$u_{i,j,k}$	Velocity component (m/s)
u_τ	Friction velocity (m/s)
$u'v'$	Velocity component fluctuations (m/s)
t	Time (s)
WJCC	Wall jet can combustor
X, Y, Z	Cartesian coordinates
x_j	Cartesian coordinates
Y^+	Dimensionless wall distance

Greek symbols

α	Coefficient in PDF equation
α_i	Diffusivity coefficient of scalar i
β	Coefficient in PDF equation
Δ	Local grid size
$\Delta X^+, \Delta Z^+$	Dimensionless cell distance

δ	Function of delta
ε	Dissipation rate of turbulence kinetic energy
η	Kolmogorov length scale
λ	Taylor length scale
Γ	Thermal conductivity (W/m K)
μ	Dynamic viscosity of continuous phase (N s/m^2)
ν	Kinematic viscosity of continuous phase (m^2/s)
ρ	Density (kg/m^3)
τ_{ij}	Stress tensor
τ_L	Large eddy time scale
τ_λ	Taylor time scale
τ_η	Kolmogorov time scale
χ	Scalar dissipation rate
ϕ_i	Scalar quantities of scalar i
$\dot{\omega}_i$	Source in scalar equation (production rate from chemical reaction)
Ω_{ij}	Rotation rate tensor
g	Gas phase (continuous phase)
d	Droplet

1 Introduction

Nowadays, computational fluid dynamics (CFD) techniques have provided a better insight into the flow and temperature fields in a combustion chamber. Various phenomena take place in a combustive flow, namely turbulence, combustion, radiant heat transfer, two-phase flow and spray. Each of these requires a suitable model to employ for simulation. Turbulence modeling is one of the most influential parts in the simulation of flow within the model combustion chamber, and currently, the Reynolds-averaged Navier–Stokes (RANS) and the large eddy simulation (LES) approaches are applied. The use of either of these two approaches depends on the objective parameters, the accuracy and the cost of the computations.

Distributions of various important parameters such as temperature, velocity, fuel droplets, concentrations of combustion species (i.e., CO_2, H_2O), pollutants (i.e., nitrogen oxides, soot), coherent structures and recirculation zones can be utilized from the flow simulations in a combustor. Some of these are captured by using both the RANS and LES approaches and some by only one. Khodabandeh et al. [1] and Alemi and Rajabi Zargarabadi [2] have employed RANS to investigate the temperature, axial velocity, O_2 and NO concentrations and have obtained appropriate results. Bazdidi-Tehrani et al. [3] have applied RANS and the flamelet combustion model for the investigation of the reactive turbulent flow in a gas turbine model combustor and have predicted the distributions of mean temperature and mean velocity with a maximum deviation of 22% in comparison with the available experimental data [4]. However, it will be shown later on in the present study that on the basis of the LES approach, the velocity and temperature distributions can be predicted with relatively lower deviations from the same experimental data.

Li et al. [5] have modeled an ethanol spray-air combustion employing the LES approach and a finite-rate filtered combustion model. Their results show LES predicts the gas temperature closer to the experimental data in comparison with using RANS and the probability density function (PDF) equation combustion model. Popov and Pope [6] have simulated a bluff body stabilized flame employing a combination of the LES and probability density function (PDF) approaches. They have stated the temperature distribution and mass fractions

of NO, OH, CO_2 and CO species in the different axial locations. Franzelli et al. [7] have studied a swirled spray flame employing LES and a 24-species chemical reaction mechanism. It has been noticed that the coupling between turbulence, spray and flame is governed by the interactions between processing vortex core, spray and flame. They have compared the mean and fluctuating gas axial velocity with the corresponding experimental data. Furthermore, the flame structure, species concentrations and pollutant emissions have been presented.

The recirculation zones are another issue that has been thoroughly investigated in the reactive turbulent flow. Because, in these zones the fuel and air are wholly mixed and complete combustion is formed. LES is a good tool for identifying the flow recirculation zones. Edge et al. [8] have reported that the recirculation zone which is influencing the flame temperature is more accurately predicted and captured by LES in comparison with the traditional RANS models.

The reason for more accurate prediction of results by LES than RANS is that in RANS all eddies are modeled, while the principal property of LES is the solution of the large-scale eddies and modeling of the small-scale eddies. The greatest amount of the turbulence energy is enclosed in the large eddy movements which are dependent on geometry, while the small-scale eddies are affected by the molecular motion and hence are much less dependent on geometry. Consequently, they are considered as universal naturally [9].

Another feature of LES is the display capability of the energy cascade from the largest turbulence length scales (integral length scale) at the lower spectrum frequencies to the smallest length scales. Jones et al. [10] have reported the distributions of mean and fluctuating velocity and temperature together with power spectral density of the temporal autocorrelation function in the simulation of a premixed swirl burner using LES and the Eulerian stochastic field method.

RANS has a limitation in providing the unsteady information, whereas LES addresses this issue [11]. However, its computational cost is much more than that of RANS. Achieving high accuracy results when using LES depends on considering the required fundamentals to solve the equations. Employing an appropriate mesh on the geometry and selecting a proper time step are the most important fundamentals to solve the problem by using LES, which have been specifically addressed in this study. Taking into account these necessary fundamentals leads to increasing the complexity, time and cost of computations. Therefore, as mentioned earlier, the use of LES or RANS depends on the objective parameters and the amount of computational cost.

LES is an appropriate tool to identify the coherent turbulent structures. One of the most complex issues in the investigation of the turbulent flow is the coherent vortical structures. Turbulence is not just about random small scales. It also includes coherent spatial structures. Since incoherent structures disappear much faster than coherent ones, coherent structures play a more important role in transmitting turbulent characteristics.

Coherent structures are three-dimensional regions of the flow over which at least one of the main variables of the flow (components of velocity, temperature, density, etc.) displays substantial correlation with another variable of the flow or with itself in the ranges of time and place. They are also meaningfully larger than the smallest local scales of the flow [12]. Theodorsen [13] has introduced these structures as three-dimensional flow patterns that are responsible for momentum and heat transfer. There are several coherent structures in the turbulent flow, namely counter-rotating, horseshoe, wake, leading edge and hairpin vortices. The definition of each of these structures is mentioned in detail in the relevant turbulence research [12, 13].

Xu et al. [14] have noticed that the Q-criterion is suitable for studying the vortex structure and evolution. To identify the coherent structures, velocity fluctuations need to be accurately

calculated. Since the RANS equations are limited in the calculation of velocity fluctuations and also eddies are modeled (not solved) in RANS, it is possible to analyze these types of structures in the turbulence modeling approaches such as LES.

Bross et al., [15] have investigated the interaction of coherent flow structures in adverse pressure gradient turbulent boundary layers. They have observed that streamwise vortex filaments of sufficient intensity must be present at small wall distances and they must be located inside or near the retarded low-speed streaks to produce a sufficiently strong spanwise motion. When these particular vortices are slightly tilted with respect to the streamwise direction due to the meandering of the streaks, for instance, they can produce reverse flow with a significant spanwise velocity component.

In the last decade, the study of these structures in the jet cooling streams has been of great interest to researchers [16]. Zamiri et al. [17] have simulated the turbulent flow structures and film cooling effectiveness in a laidback fan-shaped hole by the LES approach. They have revealed that the cooling jet flow structures and forest of hairpin vortices on the flat plate are significantly changed due to the blowing ratio. Shangguan [18] has concluded that there are qualitative and quantitative relationships between the coherent structure dynamics and heat transfer features in the flat plate film cooling. The breakdown of coherent structures is a symbol of poor cooling performance.

Considering that there are also air intake jets in the combustor and they collide with the fuel and the main swirled air flow, the study of coherent structures can be interesting and beneficial. Also, no specific study has been reported in this regard up to now.

On the basis of the above literature review, many researchers have employed LES and RANS for the simulation of turbulent flow in the gas turbine combustors. Most of the previous studies have been limited to the distributions of temperature, velocity and species concentration. However, few studies on the turbulence structures have been published concerning the spray flow in a gas turbine combustor. The main focus of the present paper is the analysis of the reactive turbulent flow structures, recirculation zones, energy cascade and turbulence length and time scales throughout the model WJCC. For this purpose, the influence of coherent vortical structures on combustion characteristics, namely temperature, velocity, scalar dissipation rate and fuel droplet diameter, is investigated. The turbulence length and time scales are used to find an appropriate mesh on the geometry and a suitable time step to ensure the simulation results. Verifications of the results are accomplished employing comparisons between (1) the mean axial velocity profiles of reactive and non-reactive flows and available experimental data and (2) the mean temperature distributions and existing experiment, at three different axial positions of the model combustor.

2 Mathematical descriptions and numerical models

2.1 Gas phase

The reactive flow equations are resolved employing the large eddy simulation (LES) approach. By applying a specified cut-off filter operation to the instantaneous governing equations (i.e., mass, momentum and scalar equations), the subsequent Favre-filtered governing equations are achieved for the resolved fields (large eddies) [19]:

$$\frac{\partial \overline{\rho}}{\partial t} + \frac{\partial \left(\overline{\rho} \tilde{u}_j \right)}{\partial x_j} = \widetilde{S}_c \tag{1}$$

$$\frac{\partial(\overline{\rho}\tilde{u}_i)}{\partial t} + \frac{\partial\left(\overline{\rho}\tilde{u}_i\tilde{u}_j\right)}{\partial x_j} = \frac{\partial}{\partial x_i}\left(\overline{\mu}\left(\frac{\partial\tilde{u}_i}{\partial x_j} + \frac{\partial\tilde{u}_j}{\partial x_i}\right) - \frac{2}{3}\left(\overline{\mu}\left(\frac{\partial\tilde{u}_k}{\partial x_k}\right)\delta_{ij}\right)\right) - \frac{\partial\tilde{P}}{\partial x_i} + \frac{\partial\tau_{ij}^{sgs}}{\partial x_j} + \tilde{F}_i$$

(2)

$$\frac{\partial\left(\overline{\rho}\widetilde{\phi}_i\right)}{\partial t} + \frac{\partial\left(\overline{\rho}\tilde{u}_j\widetilde{\phi}_i\right)}{\partial x_j} = \frac{\partial}{\partial x_j}\left(\overline{\rho}\tilde{\alpha}_i\frac{\partial\widetilde{\phi}_i}{\partial x_j}\right) + \frac{\partial q_\phi^{sgs}}{\partial x_j} + \overline{\rho}\widetilde{\omega}_i + \widetilde{S}_{\phi_i} + \widetilde{S}.$$

(3)

In these equations, $\tilde{u}_i$, P and ρ are the velocity vector, pressure and density of the gas phase, respectively. ϕ_i and α_i signify the scalar quantities and the diffusivity of the scalar i, successively. $\dot{S}_c$ and $\dot{S}_{\phi_i}$ represent the exchange terms of mass and scalars quantities between the gas and liquid phases, respectively.

The instantaneous small-scale portions are eliminated by the filter, but their impacts stay in the unclosed remaining terms signifying the effect of the sub-grid scale (SGS) on the resolved scales [20–22]. The influence of the small eddies emerges in the resolved flow field via the SGS turbulent stress tensor, τ_{ij}^{sgs}, and in the scalar field, q_ϕ^{sgs}, which are unknown and must be modeled. In the present simulation, due to the existence of rotational zones in the vicinity of the wall and wall-bounded flow in the combustion chamber, the WALE (wall-adapting local eddy viscosity) model [23] together with the Boussinesq hypothesis [21] is employed to model the SGS stress tensor.

$$\tau_{ij}^{sgs} = \overline{\rho}\tilde{u}_i\tilde{u}_j - \overline{\rho\widetilde{u_iu_j}} = \frac{1}{3}\tau_{kk}^{sgs}\delta_{ij} - 2\overline{\mu}_{sgs}\tilde{S}_{ij}$$

(4a)

$$\tilde{S}_{ij} = \frac{1}{2}\left(\frac{\partial\tilde{u}_i}{\partial x_j} + \frac{\partial\tilde{u}_j}{\partial x_i}\right)$$

(4b)

where μ_{sgs} denotes the sub-grid-scale turbulent viscosity and $\tilde{S}_{ij}$ is the rate of strain tensor for the resolved (large) scale. The sub-grid turbulent fluxes of scalars are approximated employing the gradient diffusion hypothesis [24]:

$$q_\phi^{sgs} = \overline{\rho}\tilde{u}_i\widetilde{\phi}_j - \overline{\rho\widetilde{u_i\phi_j}} = \overline{\rho}\tilde{\alpha}_{sgs}\frac{\partial\widetilde{\phi}_j}{\partial x_j}$$

(5)

where the sub-grid-scale diffusivity of scalars (α_{sgs}) is achieved based on a ratio of μ_{sgs} to sub-grid-scale Schmidt number (Sc_{sgs}) or Prandtl number (Pr_{sgs}).

2.1.1 Combustion model (turbulence–chemistry interaction)

In the turbulent reactive flows, there are a large number of reactions and species in a typical chemical kinetic mechanism. Therefore, solving the species conservation equation directly and employing the detailed chemical reaction mechanism are exceedingly time-consuming from a computational cost viewpoint [25]. Thus, on the basis of the recent works by Bazdidi-Tehrani et al. [3] and Yen, Magi and Abraham [26], the laminar flamelet model [27] as well as 17 species and 26 reduced reaction mechanism of kerosene fuel [3, 28] has been applied for the combustion modeling.

In the laminar flamelet combustion model [27], a turbulent non-premixed flame is considered as a statistical set of laminar thin flames (flamelets) [29]. Since the reaction specific time is usually small (i.e., mixing is controlling the flame phenomena), the combustion chemistry is very active in a thin layer denoted as the reaction zone. If this layer, as compared with the smallest flow scale which is the Kolmogorov eddy scale, is thin, it can be assumed that combustion is surrounded by a quasi-laminar flow and the laminar flamelet assumption is correct. When the Kolmogorov eddy scale is of the order of flame thickness, the reaction

zone may be changed by the turbulence. Also, it can disturb the flame layer structure and there is a probability of extinction.

Thus, with the theory assumed for the flamelet model, the turbulent mixing and chemistry processes can be computed distinctly in a way that the structure of the reaction region stays laminar [29].

The fundamental theory of this combustion model lies on the assumptions that the instantaneous thermochemical state of the fluid (e.g., species mass fractions and temperature) may be related to a conserved scalar known as the mixture fraction, f [27, 30]. A flamelet database, containing thermochemical quantities (species mass fraction and temperature), is formed as the functions of non-equilibrium quantity of scalar dissipation rate, mixture fraction and enthalpy [31].

In order to consider the effect of SGS turbulence fluctuations on the acquired instantaneous thermochemical quantities, the Favre sub-grid probability density function (PDF) [30] is employed:

$$\tilde{\phi}_i = \int_0^1 \phi_i\left(f, \widetilde{H_s}, \tilde{\chi}_{st}\right) p(f) df \tag{6}$$

$$p(f) = \frac{f^{a-1}(1-f)^{\beta-1}}{\int f^{a-1}(1-f)^{\beta-1} df} \tag{7a}$$

$$a = \tilde{f}\left[\frac{\tilde{f}\left(1-\tilde{f}\right)}{\widetilde{f'^2}} - 1\right] \tag{7b}$$

$$\beta = \left(1-\tilde{f}\right)\left[\frac{\tilde{f}\left(1-\tilde{f}\right)}{\widetilde{f'^2}} - 1\right] \tag{7c}$$

where H_s is the sensible enthalpy, $\tilde{\chi}_{st}$ is the mean scalar dissipation rate at stoichiometric conditions and $\tilde{f}$ and $\widetilde{f'^2}$ indicate the sub-grid Favre averaged and variance of mixture fraction, respectively. The $\widetilde{H_s}$ and $\tilde{f}$ are achieved by using the scalar conservation Eq. (3).

$$\frac{\partial\left(\overline{\rho}\tilde{f}\right)}{\partial t} + \frac{\partial\left(\overline{\rho}\tilde{u}_j\tilde{f}\right)}{\partial x_j} = \frac{\partial}{\partial x_j}\left(\overline{\rho}\widetilde{D}_f\frac{\partial\tilde{f}}{\partial x_j}\right) + \frac{\partial q_f^{sgs}}{\partial x_j} + \widetilde{\dot{S}}_f \tag{8}$$

$$\frac{\partial\left(\overline{\rho}\widetilde{H_s}\right)}{\partial t} + \frac{\partial\left(\overline{\rho}\tilde{u}_j\widetilde{H_s}\right)}{\partial x_j} = \frac{\partial}{\partial x_j}\left(\overline{\rho}\widetilde{D}_H\frac{\partial\widetilde{H_s}}{\partial x_j}\right) + \frac{\partial q_{H_s}^{sgs}}{\partial x_j} + \widetilde{\dot{S}}_{H_s} + \widetilde{\dot{S}}_r \tag{9}$$

where $q_f^{sgs} = \overline{\rho}\frac{\mu_{sgs}}{Sc_{sgs}}\frac{\partial\tilde{f}}{\partial x_j}$, $q_{H_s}^{sgs} = \frac{\mu_{sgs}}{Pr_{sgs}}\frac{\partial\widetilde{H_s}}{\partial x_j}$ and $\dot{S}_r$ is the source term due to the radiation heat transfer modeled by the discrete ordinates model (DOM) [32, 33]. The $\tilde{\chi}_{st}$ and $\widetilde{f'^2}$ are modeled as:

$$\tilde{\chi}_{st} = C_\chi\frac{(\mu + \mu_{sgs})}{\rho Sc_{sgs}}\left|\frac{\partial\tilde{f}}{\partial x_i}\right|^2 \tag{10}$$

$$\widetilde{f'^2} = C_{f-var}L_s^2\left|\frac{\partial\tilde{f}}{\partial x_i}\right|^2 \tag{11}$$

where C_χ and C_{f-var} are constants and L_s is the sub-grid length scale.

2.2 Dispersed phase

According to the recently published works [2, 34] concerning the simulation of dilute sprays, as in the present paper, the Eulerian–Lagrangian approach [35] is employed. The equations of the gaseous phase and liquid droplet phase are solved in terms of the Eulerian and Lagrangian approaches, respectively. Considering the negligible effects of gravity, Brownian and Saffman's lift forces, the path of a droplet movement is obtained from the equation of motion on the basis of the Newton's second law [36]:

$$\frac{du_d}{dt} = \frac{3\rho C_D |u_d - u|}{4\rho_d d_d}(u - u_d) \qquad (12)$$

where d as a subscript indicates a property of droplet and C_D is the drag coefficient and estimated from the proposed formula by Morsi and Alexander [37].

The effect of a turbulent flow on the distribution and dynamics behavior of droplets in the gas phase is considered by employing the random walk model [38]. The two-way coupling [39] is used to address the influence of the droplet phase on the gas phase.

The heat conversations between the gas phase and fuel droplets are considered using inert heating, evaporation and boiling of droplet. These exchange processes are specified by the vaporization and boiling temperatures. In the first step (inert heating), there is no exchange of mass between liquid and gas phases and the temperature of the droplets just increases up to the vaporization temperature:

$$m_d c_p \frac{dT_d}{dt} = hA_d(T_g - T_d) \qquad (13)$$

where h as the heat transfer coefficient is estimated by employing the empirical correlation of Ranz and Marshall [40]:

$$Nu = \frac{hd_d}{k_g} = 2.0 + 0.6\text{Re}_d^{1/2}\,\text{Pr}^{1/3}. \qquad (14)$$

Re denotes the relative Reynolds number and it is defined as $\text{Re} = \frac{\rho d_d |u_d - u|}{\mu}$. Through the second process, the droplet temperature reaches the vaporization temperature and the mass is transported from the liquid to the gas phase. The change in the droplet mass ($\frac{dm_d}{dt}$) for a high evaporation rate is expressed as in the following relation [36]:

$$\frac{dm_d}{dt} = \pi d_p \rho_g D_{i,m}\left(2 + 0.6Re_d^{1/2}Sc^{1/2}\right)ln(1 + B_m) \qquad (15)$$

where $D_{i,m}$ is the diffusion coefficient of vapor in the gas phase and B_m represents the Spalding mass transfer number. At this step, the temperature of droplet is updated by adding the latent heat transfer term to Eq. (13) and modifying the convective heat transfer coefficient.

$$m_d c_{p,d} \frac{dT_d}{dt} = hA_d(T_\infty - T_d) - \frac{dm_d}{dt}h_{fg} \qquad (16)$$

$$Nu = \frac{hd_d}{k_\infty} = \frac{Ln(1 + B_T)}{B_T}\left(2.0 + 0.6Re_d^{1/2}Pr^{1/3}\right) \qquad (17)$$

where B_T is the Spalding heat transfer number. When the temperature of droplet reaches the boiling point (as third step), the evolution of droplet size is computed by a boiling rate equation, as follows:

$$\frac{d(d_d)}{dt} = \frac{4\Gamma_g}{\rho_d C_{p,g} d_d}(1 + 0.23\sqrt{Re_d}) \times ln\left[1 + \frac{C_{p,g}(T_g - T_d)}{h_{fg}}\right]. \qquad (18)$$

Table 1 Numerical schemes

Pressure–velocity coupling algorithm	SIMPLE-C algorithm
Concentrations and turbulence quantities	Second-order upwind
Time marching (temporal discretization)	Second-order implicit
Time step, Δt	1×10^{-5} s
Sampling time	$4s (\approx 80,000$ time steps)
Spatial discretization	Bounded central differencing

More information about the spray modeling and discrete phase equations is provided in reference [41].

3 Computational methodology

3.1 Numerical methods

The present numerical simulation is implemented based on the three-dimensional finite volume method (FVM) [42], employing the unsteady SIMPLE-C algorithm [42] for resolving the collection of governing equations along with the discrete ordinates model (DOM) [32] and flamelet model [27]. The Eulerian and Lagrangian approaches along with a two-way coupling are adopted for predicting flow characteristics of the gas and liquid phases. A total of 200 discrete directions with the weighted sum of gray gases model (WSGGM) [43] are used for the computation of the radiative transfer equation by DOM.

In order to exactly capture the progress of the flow features, a physical time step of $\Delta t = 1 \times 10^{-5}$ is applied for each grid such that the Courant–Friedrichs–Lewy (CFL) number is sustained at 0.48 to prevent any numerical instability. At each time step of simulation, convergence is assumed to attain when the normalized residuals approach 10^{-5} for the continuity equation and 10^{-6} for energy, momentum, combustion, thermal radiation and species equations. A bounded central differencing scheme [44] is applied for the spatial discretization. The second-order upwind scheme [45] is employed for the concentration and turbulence quantities. Finally, the algebraic multi-grid approach together with the second-order implicit point Gauss–Seidel methods is taken on to solve the discretized equations in an iterative procedure (i.e., time marching) [46]. The details of the present numerical schemes are summarized in Table 1.

3.2 Computational domain and grid resolution assessment

The present computational domain concerning the model wall jet can combustor (WJCC) geometry is adopted based on the experimental setup of Cameron et al. [4], as illustrated in Fig. 1.

The model WJCC geometry consists of an octagon with the dimension, D = 80 mm as the diameter and 4D as the length. 163 kg/h air flow enters the combustor at 1 atm. 25%, 35% and 40% of incoming air are introduced into the combustor through an axial type of swirler, primary and dilution holes, consecutively. Details of the relevant flow and geometrical data regarding WJCC are listed in Table 2.
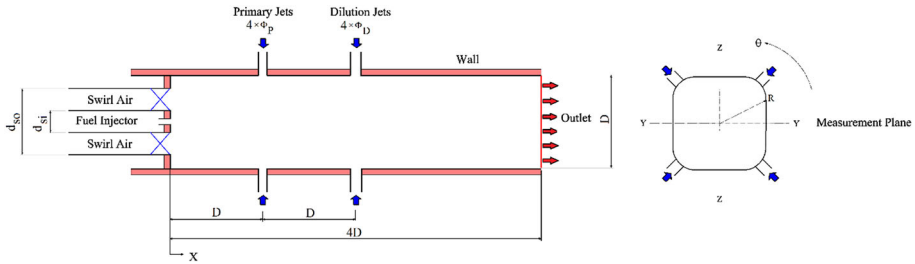
Fig. 1 Schematic representation of model WJCC and boundary conditions

Table 2 Geometrical and flow specifications of WJCC

Parameter	Value
Fuel mass flow rate (kg/h)	3.27
Fuel cone angle (°)	60
Fuel/air relative velocity (m/s)	110
Fuel temperature (K)	300
Type of fuel	Kerosene
Operating pressure (atm)	1
Swirler diameter (m)	Inside: 0.019; outside: 0.057
Swirl number	1.4
Primary holes diameter (m)	0.007
Dilution holes diameter (m)	0.0095

Due to the unavailability of the experimental inlet velocity data and, consequently, the impossibility of an initial estimation of the number of inlet vortices, the inlet mass flow is considered as the entrance boundary condition. At exit plane of the cross flow, pressure outlet boundary condition is employed. Also, the thermal and velocity boundary conditions in all of the walls are assumed as adiabatic and no-slip, successively. For the radiation heat transfer, the emissivity of the walls is assumed to be 0.7.

In order to determine a proper grid resolution, the computational domain of WJCC is discretized into 1,279,488, 1,807,024 and 3,050,046 hexahedral non-uniform computational cells for the coarse, medium and fine grids, respectively. The suitability of the grid resolution is evaluated by using the two-point correlation technique which has recently been examined in details by Bazdidi-Tehrani et al. [20]. It is based on the ratio of SGS shear stress to resolved shear stress and the ratio of SGS viscosity to molecular viscosity. It is detected that nearly 12 cells have been adequately included in the lateral integral length scale. The applied grid should take account of three necessary conditions (criteria) for implementing the LES approach:

$$\left(Y^+ = \frac{Y u_\tau}{\nu} < 1 \right), \left(\Delta X^+ = \frac{\Delta X u_\tau}{\nu} < 40 \right) \text{ and } \left(\Delta Z^+ = \frac{\Delta Z u_\tau}{\nu} < 20 \right). \qquad (19)$$

The above-mentioned conditions have been fulfilled for the fine grid. Thus, the fine grid is adopted throughout the present work (Fig. 2). Grids adjacent to the walls are chosen to be finer, particularly near the air jet holes and at the entrance of the combustor, owing to the existence of a reverse flow and the combustion phenomenon. Away from the dilution holes,
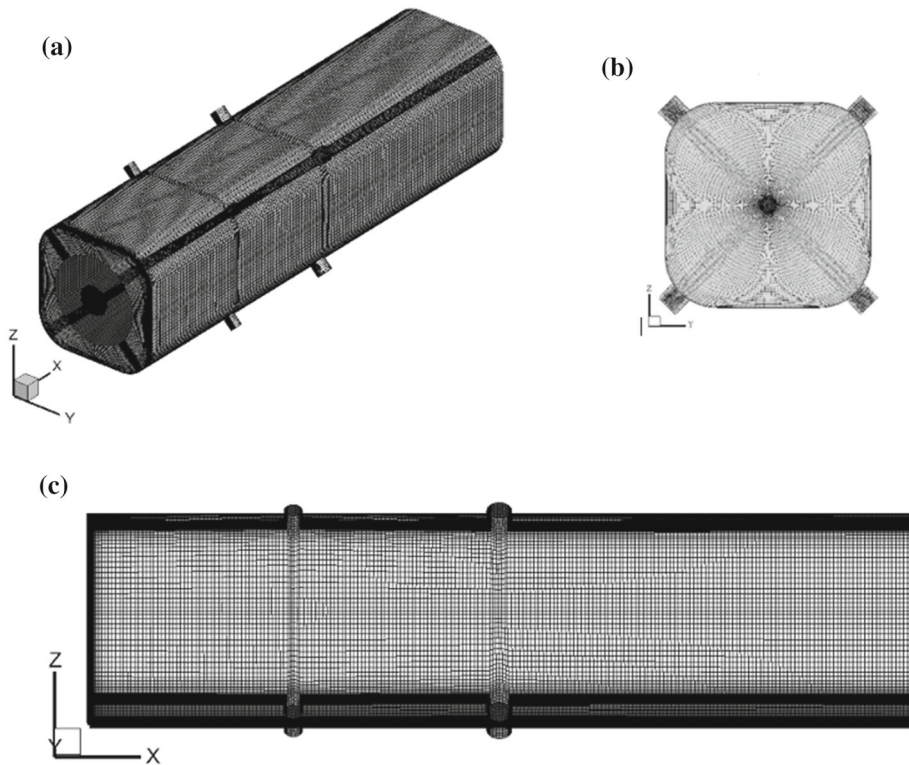
Fig. 2 Structured mesh on model WJCC: **a** XYZ plane, **b** X = 0 plane and **c** Y = 0 plane

the cell size is increased by a growth factor of around 1.06 so as to limit the commutation error [47].

3.3 Evaluation of turbulence length and time scales

The filter width is presently assumed as the turbulence length scale and computed by employing the local grid size as $\Delta = (\Delta_X \Delta_Y \Delta_Z)^{1/3}$. The other length scales including the Kolmogorov length scale ($(\eta = (v^3/\varepsilon)^{1/4})$), Taylor length scale ($\lambda = (10vk/\varepsilon)^{1/2}$) and integral length scale ($L = (k^{3/2}/\varepsilon)$) [9, 48] are also computed. Figure 3 shows a comparison of the filter width (Δ) with different turbulence length scales in the mid-plane (Y = 0) of WJCC. It is observed that the filter width is about one-tenth of the integral length scale (i.e., turbulence length scale of large eddies) and lies between the Kolmogorov and Taylor length scales. This is in line with the work reported by Baggett et al. [49]. Therefore, the present simulation can apply the various turbulence length scales. This issue is depicted in a different way in Fig. 10 later on representing the power spectrum density (PSD) functions [21] of the axial velocity fluctuations.

Choosing an appropriate time step (Δt) is very important along with considering an unsteady calculation in the LES approach. With a decrease in the time step, the accuracy of the computation turns out to be higher. However, this will lead to a large increase in the overall time and cost of computing. Generally, the time step is chosen in the range of the time required to pass the flow from the smallest computing domain. In order to accurately solve and detect
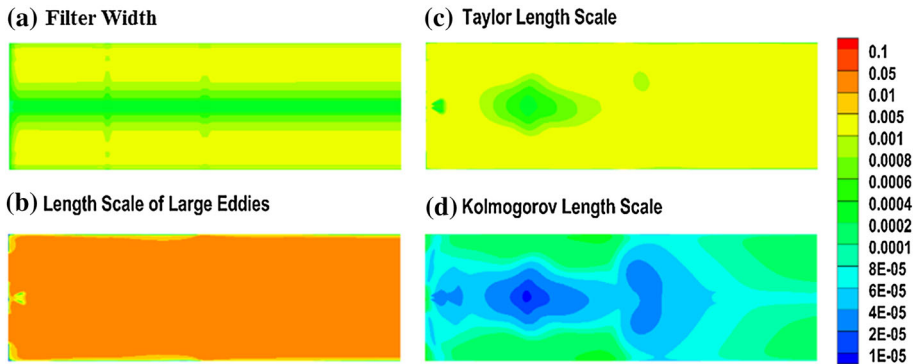
(a) Filter Width

(c) Taylor Length Scale

(b) Length Scale of Large Eddies

(d) Kolmogorov Length Scale

Fig. 3 Comparison of filter width with three various turbulence length scales in mid-plane plane (Y = 0) of WJCC

the flow structures, a physical time step should be selected such that the maximum value of CFL $= \frac{u\Delta t}{\Delta X}$ becomes less than 1.0 for the computational domain [50]. This is necessary to prevent any numerical instabilities. Also, it is suggested that the maximum CFL be equal to 0.5 in the LES approach [51]. On the other hand, the time step should be chosen in such a way that the time scale of the resolved eddies be much smaller than the large eddy time scale $(\tau_L = k/\varepsilon)$ and also less than the Taylor time scale $\left(\tau_\lambda = (15v/\varepsilon)^{1/2}\right)$ and Kolmogorov time scale $(\tau_\eta = (v/\varepsilon)^{1/2})$ [52]. With these limitations, $\Delta t = 1 \times 10^{-5}$ is considered for the time step. Figure 4 depicts the different turbulence time scales in the mid-plane (Y = 0) of WJCC. Accordingly, the presently applied time step is much less than that of the large eddy (integral) time scale and smaller than those of the Taylor and Kolmogorov time scales.

4 Results and discussion

In order to confirm the validity of the present numerical scheme, the computed mean axial velocity (u) and mean temperature (T) are compared with those of the available experimental data [4], as displayed in Figs. 5 and 6, respectively. These are carried out at several different axial positions along WJCC for the reactive and non-reactive flows. It should be mentioned that a non-reactive flow means an isothermal flow, in the absence of liquid fuel injection. From Fig. 5 representing the numerical mean axial velocity (Y-axis) versus the experimental one (X-axis), it can be seen that the numerical results are in reasonable agreement with the experimental data and the maximum deviations of 6% are detected at X = 0.1 m for the reactive flow. Due to a higher density of the gas phase in the non-reactive flow, the mean axial velocity is lower than the one in the reactive flow, at all the three positions. Owing to the formation of a reverse flow caused by the swirler, the velocity at X = 0.04 m for both the reactive and non-reactive flows is less than those at the two other positions. However, a small reverse flow is seen at X = 0.1 m with by viewing the negative values of mean axial velocity. The reverse flow is discussed more in Fig. 7. The numerical mean temperature at three axial positions is compared with the available experimental data in Fig. 6. It is observed that a credible agreement with negligible deviations exists (i.e., a maximum of 5% at all X).

Figure 7 depicts the distributions of the velocity vectors along the mid-plane (Y = 0). The size of the vectors represents the value of the instantaneous flow velocity. Three main recirculation zones are detected and displayed by parts (a) to (c). The first one (Fig. 7a), which
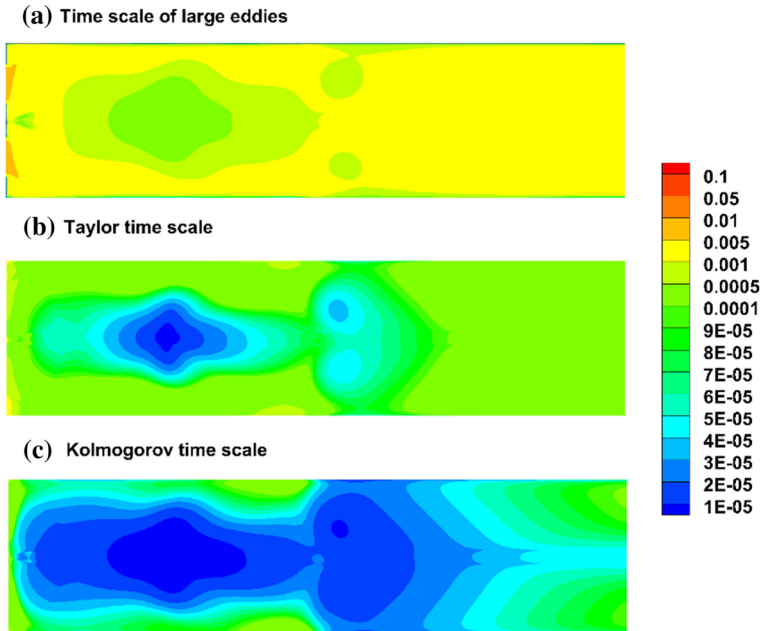
Fig. 4 Comparison of three different turbulence time scales in the mid-plane (Y = 0) of WJCC

covers a small region, is close to the entrance side walls of the model WJCC. The second one (Fig. 7b) is formed adjacent to the primary jets which occupies a large area. The third one (Fig. 7c) is shaped up in the center of the model combustor immediately after the locations of the dilution jets. The recirculation zone plays a significant role in the flame stability inside the combustion chamber. The reverse flow is mainly influenced by the collision of swirl flow and outflow of air jets. The maximum and minimum flame temperatures are totally dependent on these recirculation zones (refer to Fig. 9).

Figure 8 displays the contours of time-mean axial velocity across the mid-plane of the model WJCC at three lateral cross sections of X = 0.07 m, X = 0.09 m and X = 0.18 m. The same as the velocity vectors in Fig. 7, the recirculation zones may be detected from the distributions of the streamlines. On the mid-plane, the streamlines are plotted on the mean velocity contour. At the lateral cross section of X = 0.07 m, the effect of the presence of a large flow reversal due to the primary jets is demonstrated by a blue color region. At X = 0.09 m and X = 0.18 m which refer to the locations immediately after the primary and dilution jets, respectively, under the influence of incoming air jets and back reverse flow, a higher velocity zone resulting from a larger axial flow is observed in the center of the cross sections. In the intermediate zone (i.e., between the primary and dilution holes), the flow velocity is higher due to a greater mass flow rate of the incoming air through the primary jets and the smaller diameter of the primary holes, as compared with the dilution holes. The velocity distribution becomes uniformly toward the end regions of WJCC.

Figure 9 shows the mean static temperature contours across the mid-plane (Y = 0) of WJCC at three different cross sections, namely X = 0.01 m, X = 0.07 m and X = 0.18 m. In the central cross section of X = 0.01 m, a blue color point can be seen because of the presence of the liquid fuel and heat transfer from the gas phase to liquid phase so as to

Fig. 5 Numerical mean axial
velocity of reactive and
non-reactive flows (Y-axis) versus
experimental mean axial velocity
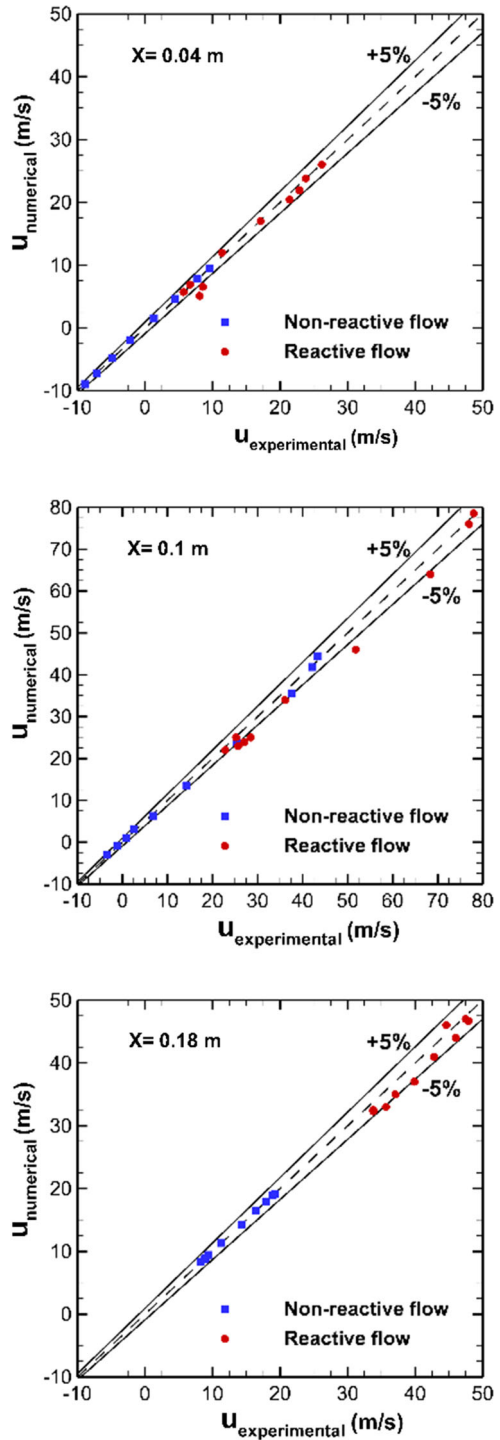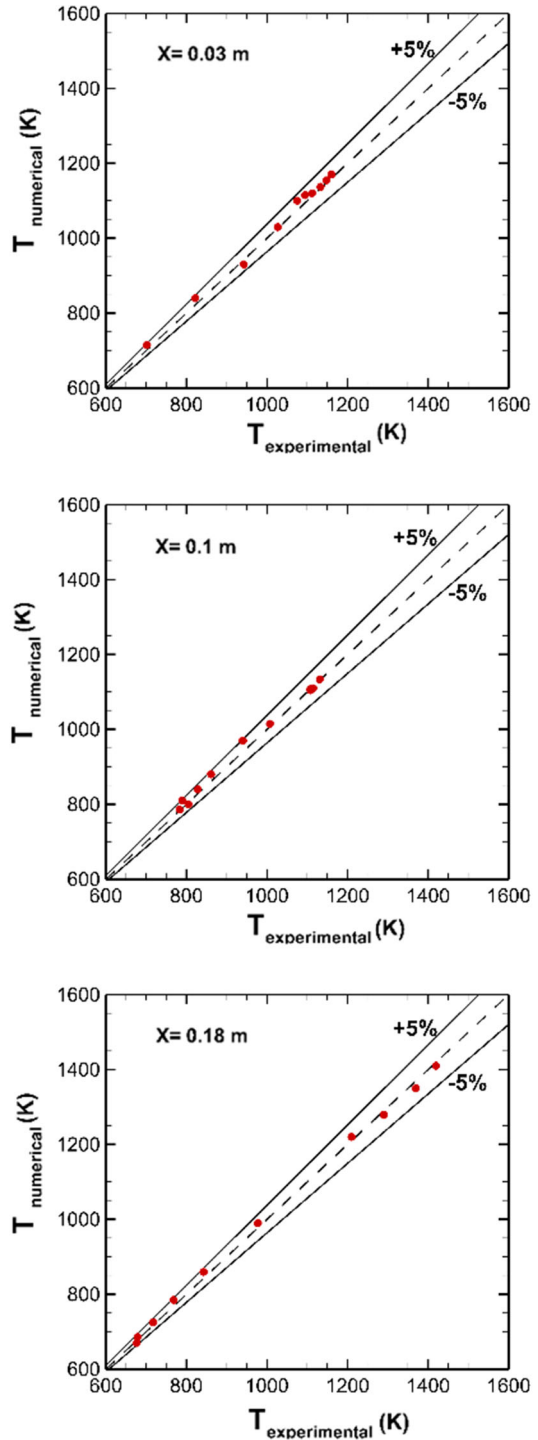of Cameron et al. [4] (X-axis), at
three different axial positions

Fig. 6 Numerical mean temperature (Y-axis) versus experimental mean temperature of Cameron et al. [4] (X-axis), at three different axial positions

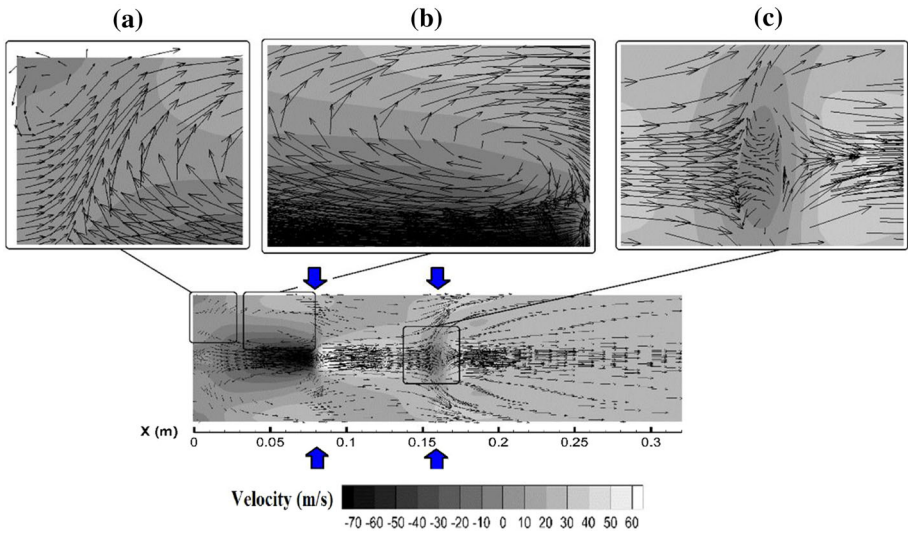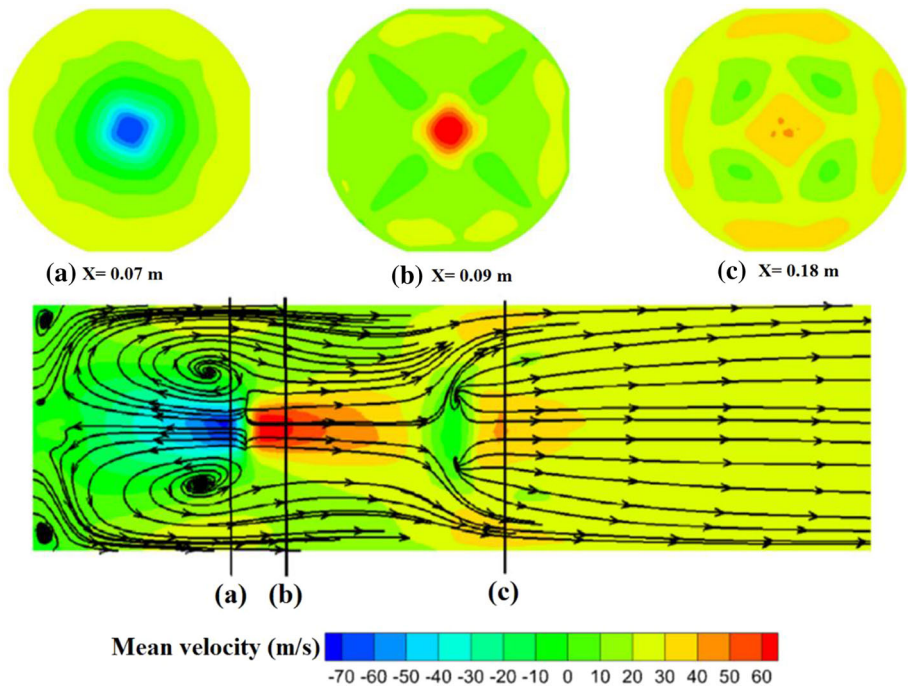**Fig. 7** Distributions of velocity vectors along mid-plane (Y = 0)

Fig. 8 Contours of time-mean axial velocity across mid-plane (Y = 0) of WJCC at three lateral cross sections: **a** X = 0.07 m, **b** X = 0.09 m and **c** X = 0.18 m

evaporate the droplets. The effects of both the swirling air and the onset of combustion reactions are detected and displayed by the blue and yellow rings, respectively.
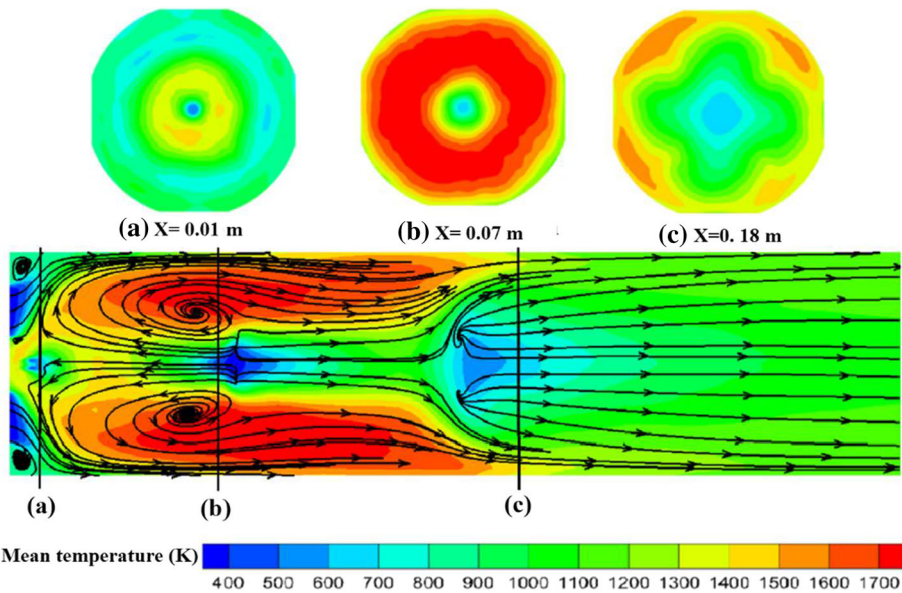
Fig. 9 Contours of time-mean temperature across mid-plane (Y = 0) of WJCC at three lateral cross sections: **a** X = 0.01 m, **b** X = 0.07 m and **c** X = 0.18 m

At X = 0.07 m, due to the presence of flow reversal, mixtures of hot gases are observed around the cross section, while, in the center of the cross section, a blue zone is illustrated as a result of the existence of the non-reactive cool gases. At X = 0.18 m, the influence of the dilution air jets and reverse flow on the formation of a uniform temperature distribution at the outlet of the combustion chamber is shown. This section is surrounded by the hot gases near the walls and the cool air in the center. However, the major portion of this section shows that the hot gases reach an equilibrium and fairly uniform temperature. It is also observed that the largest values of temperature are achieved in the region between the primary and dilution holes (intermediate zone). The maximum temperature (1700 K) occurs due to the flame trapping, under the influence of the largest reverse flow. In this zone, a complete mixing of the fuel and air is formed and the combustion reactions are developed in an enough period of time. By moving away from the dilution jets, the temperature decreases and the temperature distribution tends toward uniformity at the end of the WJCC.

Figure 10 illustrates the power spectrum density (PSD) [21] of the axial velocity fluctuations (E_{uu}), on the basis of the time series and Fourier transforms at the center of WJCC (X = 0.07 m, Y = Z = 0.0). The PSD scheme represents the energy cascade from the largest turbulence length scales (integral length scale) at the lower frequencies of the spectrum to the smallest length scales (Kolmogorov length scale) at the higher frequencies. The − 5/3 power law inertial sub-range section (Taylor length scale) plays a transforming role in the energy cascade [53]. Existence of this region clarifies that the inertial sub-range can be identified in the computational domain of WJCC. At the end, the energy of Kolmogorov length scale dissipates with a -7 slope, steeper than the − 5/3, and the frictional conversion of the kinetic to thermal energy takes place. Therefore, as discussed in Fig. 3, the present simulation can apply the various turbulence length scales.

Fig. 10 Power spectral density of axial velocity fluctuations at center of WJCC (X = 0.07 m, Y = Z = 0.0)
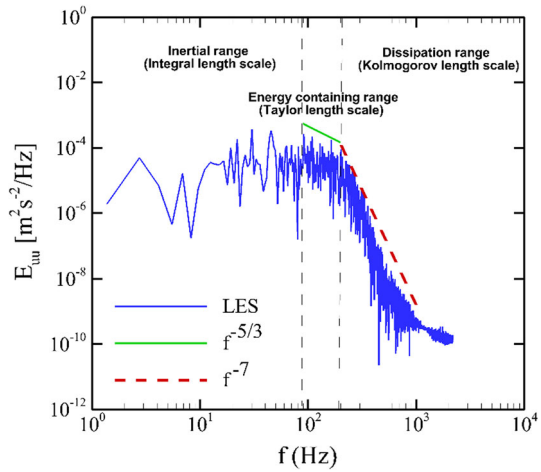
In order to detect the coherent vortical structures in the reactive turbulent flow, the second invariant of the velocity gradient tensor, called Q-criterion, is employed [54]:

$$Q = 1/2\left(\Omega_{ij}\Omega_{ij} - S_{ij}S_{ij}\right) \tag{20}$$

where Ω_{ij} is the rotation rate tensor and S_{ij} is the strain rate tensor which signify the asymmetric and symmetric parts of the velocity gradient tensor, successively. Q is considered as a balance between the strain rate and the rotation rate. Positive Q-contours represent areas in which the rotation rates are greater than the strain rates. In this section, the coherent structures and the correlations between these structures with the reactive spray flow characteristics are investigated by employing the Q criterion.

Figure 11 demonstrates the instantaneous iso-surfaces of coherent vortical structures, $Q = 5E + 07\ s^{-2}$, throughout WJCC. In this value of Q, most of the coherent structures are identifiable and colored, based on the values of temperature (K). In this reactive spray flow field, a variety of the coherent structures comprising the hairpin vortices, which are the subset of arch vortices, streamwise vortices and vortex tubes is visible. The flow in the various regions of WJCC exhibits completely different structures. For example, the flow behavior in the intermediate zone is quite different to that in the dilution zone (i.e., the zone immediately after the dilution holes). In the primary and intermediate zones the hairpin vortices and in the dilutions zone the streamwise vortices are observed more. Vortex tubes structures are one of the most basic structures known in the turbulence field. They rotate around their cores and are the foundation of the hairpin vortices structures. Streamwise structures are also a type of the vortex tube ones that are known due to the correlation between velocity along the flow and the rotation around the vortex core. However, both types of these structures have the same nature and the reason for the distinction in the naming is merely to emphasize the motion description of the structures.

Because of the occurrence of the combustion phenomenon in the primary and intermediate zones, the flow analysis of these two zones is of particular importance. As shown in Fig. 11, the hairpin vortices are observed more in the primary and intermediate zones. Therefore, hairpin vortices structures are one of the most important ones in the turbulent reactive flow. In order to identify them in the flow field of the model combustion chamber, the streamlines and the quadrant analyses, which have been introduced by Wallace et al.[55], have simultaneously been employed. According to the streamlines and the quadrant analyses, the head of hairpin
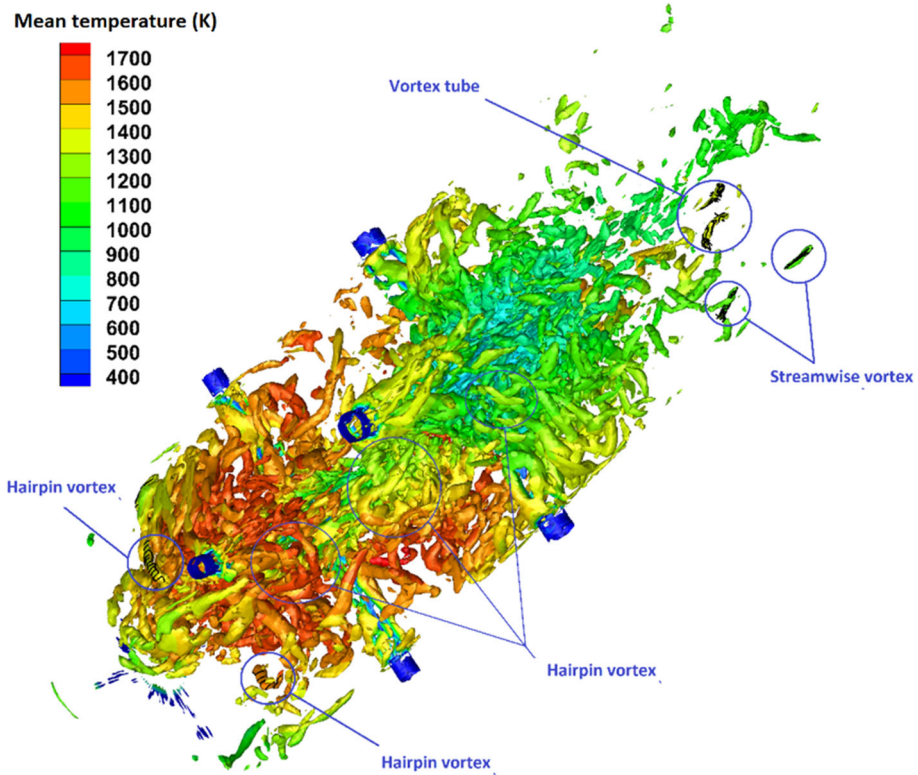
Fig. 11 Instantaneous iso-surfaces of coherent vortical structures, $Q = 5E + 07$ s^{-2}, throughout WJCC, colored based on values of temperature

vortices structures has two specific behaviors. Firstly, based on the quadrant analysis, the head has a sweep property $(u'v'\langle 0, u'\rangle 0, v' < 0)$. Secondly, by using the streamlines analysis, it is shown that the head has a twist toward the inside of the flow and the boundary layer. Figure 12 displays these behaviors in the two selected hairpin vortices. The sweep property of the vortex head as well as the streamlines confirms a twisting behavior. The sweep movement with a high momentum transfer of fluid increases the velocity gradient and the local shear stress.

A streamwise vortex which is colored by the $u'v'$ component velocity is illustrated in Fig. 13(a). It has been extracted from the dilution zone of WJCC. The light blue color represents $u'v' < 0$. The main feature of this type of coherent structure is the streamlines that are exactly in line with the main stream. Figure 13(b) and (c) displays the plotted streamlines on two vortex tube structures, which are colored by the $u'v'$ component velocity. According to the streamlines, it is shown that the structures have rotations around their axes, which is considered as their main feature.

Figure 14 displays the distribution of the fuel mean mixture fraction along the centerline of the model combustor. The amount of fuel mixture fraction is calculated by considering the mass of fuel vapor. It means that the liquid part of the fuel is not considered. The maximum point is related to the place where the highest amount of fuel vapor has been accumulated.
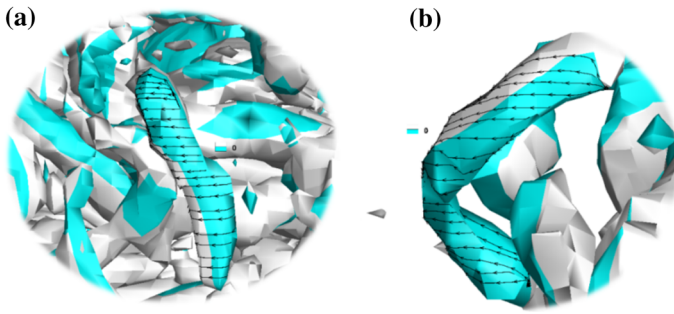
(a)   **(b)**

Fig. 12 Streamlines and quadrant analyses on two selected hairpin vortices in: **a** primary zone and **b** intermediate zone

(a)   **(b)**   **(c)**
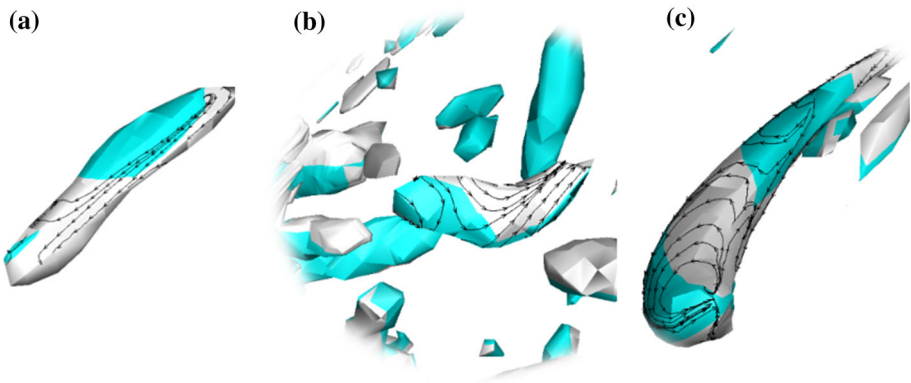

Fig. 13 Streamlines and quadrant analyses ($u'v'$ component velocity) for three selected vortical structures in dilution zone of WJCC: **a** streamwise structure, **b** and **c** vortex tube

Near the fuel nozzle, the newly formed fuel vapors react with the inlet air from the swirler and ignite. As the fuel combustion is complete and oxygen enters the primary jets, the amount of mixture fraction decreases. It is also observed that there is a small amount of fuel species up to the end of the combustor, which means that the mixture fraction is not zero.

Figure 15 shows the mass fraction distributions of species H_2O, CO_2 and O_2 on the center line of the model combustion chamber. Species CO_2 and H_2O are the main products of combustion and their distributions have an approximately similar pattern. The O_2 concentration reaches its minimum value due to the combustion process taking place in that region accompanied by oxygen consumption during the reactions. As the combustion reactions begin and intensify downstream of the fuel injector, the mass fractions of CO_2 and H_2O are increased progressively reaching their maximum values. With the arrival of species O_2 from the primary air jets, the O_2 amount increases and the mass fractions of species CO_2 and H_2O are reduced. With the continuation of combustion reactions in the recirculation zone between the primary jets and the dilution, O_2 is consumed and the mass fractions of CO_2 and H_2O species are increased again. As air enters via the dilution jets, the mass fractions of CO_2 and H_2O are decreased, similar to the mean flow temperature (Fig. 9). In this way, the reaction of

Fig. 14 Distribution of fuel mean mixture fraction along centerline
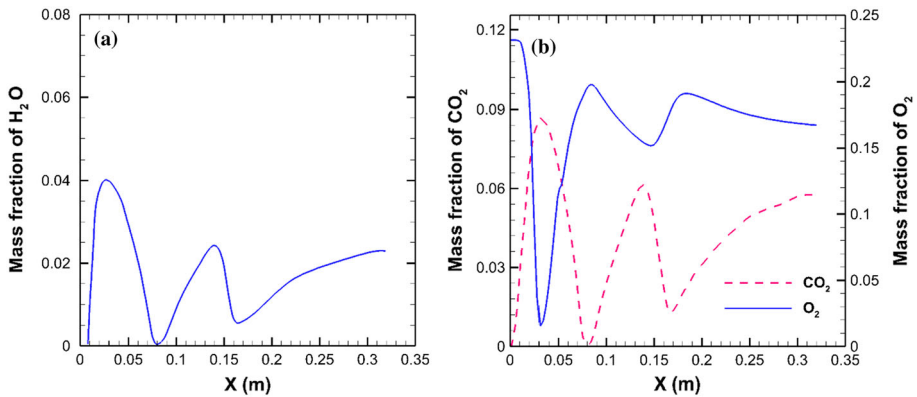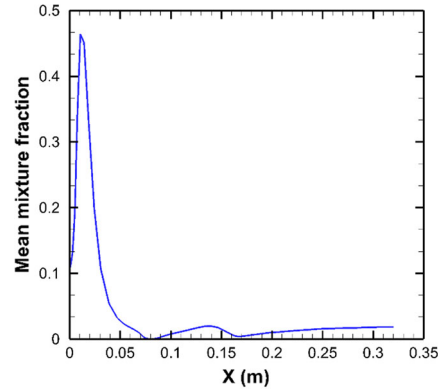
Fig. 15 Mass fraction distributions of species H_2O, CO_2 and O_2 on the centerline

the air introduced through the dilution jets with the combustion products results in a chemical equilibrium and the mass fraction of the species reaches an almost constant value at the end of the chamber.

Distributions of some variables have direct effects on distributions of the other. Therefore, in order to identify the relationship between the most important structures in the combustion chamber (hairpin) and the characteristics of the reactive spray flow, different variables including temperature, maximum scalar dissipation rate and velocity fluctuations are studied. The coherent structures or energetic large eddies play a major role in the production and control of the flow turbulence. By controlling the turbulence production mechanism, improved mixing and heat transfer, more complete combustion and less pollutants production are possible through changing the distribution and type of the coherent structures [56].

According to Fig. 16a, b where the hairpin structures are extracted from the primary and intermediate zones, respectively, a correlation between the temperature and hairpin coherent structures is found. In the head of hairpins, a significant temperature reduction is observed. This particular correlation in the turbulent flow can be important in the discussion of the wall cooling or a specific region of the combustion chamber. According to Fig. 16c, a maximum scalar dissipation rate is observed in the head of the hairpin vortices which has been extracted from the primary zone. There is, therefore, a correlation between the scalar depreciation rate
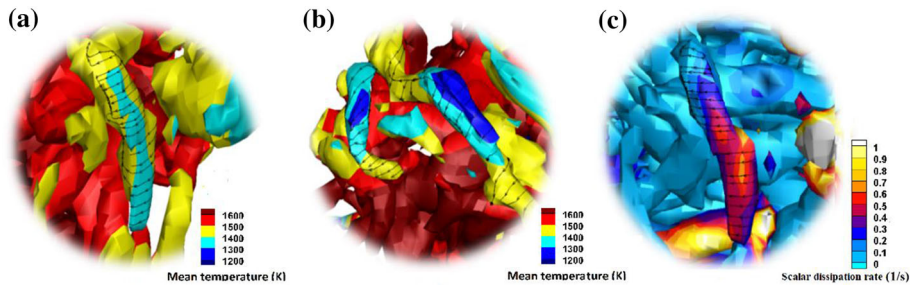
Fig. 16 Relationship between mean temperature, scalar dissipation rate and selected hairpins from **a** primary zone, **b** intermediate zone and **c** primary zone

and the hairpin vortices structures. It can be considered as one of the influential factors on the flame stability.

Figure 17 represents the iso-surface contours of the three-dimensional coherent structures along with the two-dimensional contours of the fluctuations of droplet diameter, throughout WJCC. The positive Q-contours denote the areas in which the rotation rates are greater than the strain ones. A large rotation rate can be an influential parameter regarding the break-up, collision, evaporation and, consequently, diameter variation of droplets.

At the beginning of WJCC, immediately after the swirler, a region of dense coherent structures is formed. It is one of the effective factors concerning the sharp fluctuations of the droplet diameter. In the middle regions of the chamber, densely coherent structures are also present. However, no droplets diameter fluctuations are observed. This is because evaporation of the droplets is completed before the intermediate zone (i.e., between the primary and dilution holes).

Figure 18 depicts the contours of the strain rate along with the fuel droplets, scaled 500 times bigger than the actual diameters. The strain rate is among the most important parameters relating to the flame scalar deposition rate. An increase in the strain rate can lead to weakening the flame, reducing its temperature and even its extinction. The greatest rate is visible at the center of the collision of the primary jets and the main stream. Hence, the minimum temperature is observed in that region (Fig. 9). Therefore, the strain rate and flow temperature have an inverse relationship.
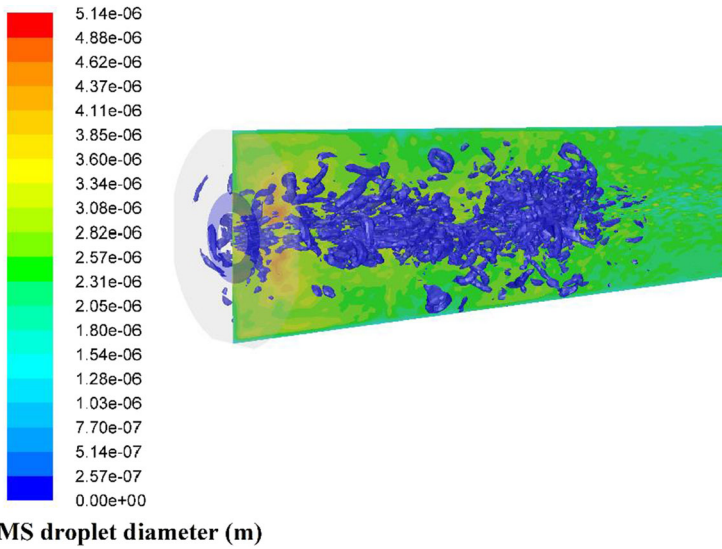
Fig. 17 Iso-surface contours of three-dimensional coherent structures ($Q = 5E + 07 \ s^{-2}$) along with two-dimensional contours of fluctuations of droplet diameter
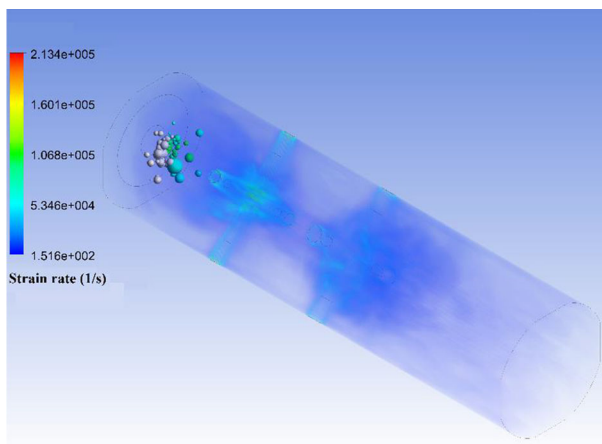

Fig. 18 Contours of strain rate along with droplets (scale: 500 times larger than actual)

5 Conclusions

In the present article, the turbulent spray flow characteristic s in a model wall jet can combustor (WJCC) are investigated by employing the large eddy simulation (LES) and Eulerian–Lagrangian approaches together with an appropriate mesh and a suitable time step.

The mean axial velocity and mean temperature are compared with the available experimental data, for both reactive and non-reactive flows, to confirm the validity of the present numerical results. Then, the influence of coherent vortical structures on the combustion characteristics, namely temperature, velocity, scalar dissipation rate and fuel droplet diameter, in the reactive flow is assessed. The main conclusions can be drawn as follows:

1. The numerical results are in reasonable agreement with the experimental data, and the maximum deviations of 6% are detected at X = 0.1 m for the mean axial velocity of the reactive flow.

2. Three main recirculation zones are observed by LES. The first one, which covers a small region, is close to the entrance side walls of the model WJCC. The second one is formed adjacent to the primary jets which occupies a large area. The third one is shaped up in the center of the model combustor immediately after the locations of the dilution jets.

3. The largest values of temperature are achieved in the region between the primary and dilution holes (intermediate zone) due to the flame trapping, under the influence of the largest reverse flow. By moving away from the dilution jets, the temperature decreases and the temperature distribution tends toward uniformity at the end of the WJCC.

4. With the continuation of combustion reactions in the recirculation zone between the primary jets and the dilution, O_2 is consumed and the mass fractions of CO_2 and H_2O species are increased.

5. The energy cascade in the spray reactive flow is achievable by employing the LES approach and power spectrum density (PSD) scheme. The energy cascades from the largest turbulence length scales (integral length scale) at the lower frequency of the spectrum to the smallest length scales (Kolmogorov length scale) at the higher frequencies. The $-5/3$ power law inertial sub-range section (Taylor length scale) plays a transforming role in the energy cascade. The energy of Kolmogorov length scale dissipates with a slope of -7.

6. A variety of the coherent structures comprising the hairpin vortices, which are the subset of arch vortices, streamwise vortices and vortex tubes is visible. The flow in the various regions of model WJCC exhibits completely different structures. In the primary and intermediate zones the hairpin vortices and in the dilutions zone the streamwise vortices are observed more.

7. A relationship between temperature and hairpin coherent structures is found. A significant temperature reduction is observed in the head of hairpins. This particular relationship in the turbulent flow can be important in the discussion of the wall cooling or a specific region of the combustion chamber.

8. A maximum scalar dissipation rate is observed in the head of the hairpin vortices. There is, therefore, a relationship between the scalar depreciation rate and the hairpin vortices structures. It can be considered as one of the influential factors on the flame stability.

9. At the beginning of WJCC, immediately after the swirler, a region of dense coherent structures is formed. It is one of the effective factors concerning the sharp fluctuations of the droplet diameter.

10. The strain rate and flow temperature have an inverse relationship. The greatest rate is visible at the center of the collision of the primary jets and the main stream, where the minimum temperature is observed.

References

1. E. Khodabandeh, H. Moghadasi, M. Saffari Pour, M. Ersson, P.G. Jönsson, M.A. Rosen, A. Rahbari, Chin. J. Chem. Eng. **28**(4), 1029 (2020)
2. E. Alemi, M.R. Zargarabadi, Int. J. Therm. Sci. **112**, 55 (2017)
3. F. Bazdidi-Tehrani, S. Mirzaei, M.S. Abedinejad, Energy Fuels **31**(7), 7523 (2017)
4. C. Cameron, J. Brouwer, C. Wood, G. Samuelsen, J. Eng. Gas Turbines Power **111**(1), 31 (1989)
5. K. Li, L. Zhou, C.K. Chan, Chin. J. Chem. Eng. **22**(2), 214 (2014)
6. P.P. Popov, S.B. Pope, Combust. Flame **161**(12), 3100 (2014)

7. B. Franzelli, A. Vié, M. Boileau, B. Fiorina, N. Darabiha, Flow Turbul. Combust. **98**(2), 633 (2017)
8. P. Edge, S.R. Gubba, L. Ma, R. Porter, M. Pourkashanian, A. Williams, Proc. Combust. Inst. **33**(2), 2709 (2011)
9. L. Davidson, *Sweden: Chalmers University of Technology* (2015).
10. W. Jones, A. Marquis, V. Prasad, Combust. Flame **159**(10), 3079 (2012)
11. L. Zhou, K. Li, F. Wang, Chin. J. Chem. Eng. **20**(2), 205 (2012)
12. S.K. Robinson, Annu. Rev. Fluid Mech. **23**(1), 601 (1991)
13. T. Theodorsen, in *50 Jahre Grenzschichtforschung* (Springer, 1955), pp. 55.
14. M. Xu, X. Yang, X. Long, Q. Lyu, B. Ji, Sci. China Technol. Sci. **61**(1), 86 (2018)
15. M. Bross, T. Fuchs, C.J. Kähler, J. Fluid Mech. **873**, 287 (2019)
16. C. Wang, J. Zhang, H. Feng, Y. Huang, Appl. Therm. Eng. **129**, 855 (2018)
17. A. Zamiri, S.J. You, J.T. Chung, Aerosp. Sci. Technol. **100**, 105793 (2020)
18. Y. Shangguan, Heat Transfer Engineering (just-accepted), 1 (2021).
19. A. Fossi, B. Paquet, S. Kalla, and J. M. Bergthorson, presented at the ASME Turbo Expo 2015: Turbine Technical Conference and Exposition, 2015 (unpublished).
20. F. Bazdidi-Tehrani, A. Ghafouri, M. Jadidi, J. Wind Eng. Ind. Aerodyn. **121**, 1 (2013)
21. S. B. Pope, (Cambridge University Press, United Kingdom, 2000).
22. F. Bazdidi-Tehrani, N. Bohlooli, M. Jadidi, Progr. Comput. Fluid Dyn. Int. J. **15**(4), 214 (2015)
23. F. Nicoud, F. Ducros, Flow Turbul. Combust. **62**(3), 183 (1999)
24. K.A. Kemenov, H. Wang, S.B. Pope, Combust. Theor. Model. **16**(4), 611 (2012)
25. B. Shahriari, M. Thomson, S. Dworkin, Presented at the ASME Turbo Expo 2015: Turbine Technical Conference and Exposition, 2015 (unpublished).
26. M. Yen, V. Magi, J. Abraham, Chem. Eng. Sci. **196**, 116 (2019)
27. H. Pitsch, N. Peters, Combust. Flame **114**(1), 26 (1998)
28. K. Kundu, P. Penko, T. VanOverbeke, AIAA **99**, 2218 (1999)
29. D. Veynante, L. Vervisch, Prog. Energy Combust. Sci. **28**(3), 193 (2002)
30. N. Peters, *Turbulent combustion*. (Cambridge University Press, 2000).
31. R. Sarlak, M. Shams, R. Ebrahimi, Proc. Inst. Mech. Eng. Part C J. Mech. Eng. Sci. **226**(5), 1290 (2012)
32. W. Fiveland, J. Heat Transfer **106**(4), 699 (1984)
33. H. Zeinivand, F. Bazdidi-Tehrani, Heat Transf. Res. **42**(6), 571 (2011)
34. F. Bazdidi-Tehrani, M.S. Abedinejad, Chem. Eng. Sci. **189**, 233 (2018)
35. F.F. Dizaji, J.S. Marshall, Powder Technol. **318**, 83 (2017)
36. P. Ghose, A. Datta, A. Mukhopadhyay, J. Therm. Sci. Eng. Appl. **8**(1), 011004 (2016)
37. G. Kohnen, M. Rüger, M. Sommerfeld, ASME-Publications-FED **185**, 191 (1994)
38. A. Berlemont, M. Grancher, G. Gouesbet, Int. J. Heat Mass Transf. **38**(16), 3023 (1995)
39. S. Morsi, A. Alexander, J. Fluid Mech. **55**(02), 193 (1972)
40. S.S. Sazhin, Prog. Energy Combust. Sci. **32**(2), 162 (2006)
41. W. A. Sirignano, *Fluid dynamics and transport of droplets and sprays*. (Cambridge University Press, 1999).
42. F.F. Dizaji, J.S. Marshall, J.R. Grant, J. Fluid Mech. **862**, 1 (2019)
43. W. Ranz, W. Marshall, Chem. Eng. Prog **48**(3), 141 (1952)
44. G. Faeth, Prog. Energy Combust. Sci. **9**(1), 1 (1983)
45. F. Bazdidi-Tehrani, M.S. Abedinejad, H. Yazdani-Ahmadabadi, Heat Transf. Res. **49**(17), 1667 (2018)
46. S. I. A. F. M. Flows and M. Sommerfeld, *Best Practice Guidelines for Computational Fluid Dynamics of Dispersed Multi-Phase Flows*. (European Research Community on Flow, Turbulence and Combustion (ERCOFTAC), 2008).
47. N. Ashgriz and J. Mostaghimi, *Fluid Flow Handbook*. (McGraw-Hill Professional, 2002).
48. T. Smith, Z. Shen, J. Friedman, J. Heat Transfer **104**(4), 602 (1982)
49. B. Leonard, Comput. Methods Appl. Mech. Eng. **88**(1), 17 (1991)
50. T. Barth and D. Jespersen, presented at the 27th Aerospace sciences meeting, 1989 (unpublished).
51. H. K. Versteeg and W. Malalasekera, *An Introduction to Computational Fluid Dynamics: The Finite Volume Method*. (Pearson Education, 2007).
52. M. Jadidi, F. Bazdidi-Tehrani, M. Kiamansouri, J. Build. Perform. Simul. **11**(2), 241 (2018)
53. A.L. Marsden, O.V. Vasilyev, P. Moin, J. Comput. Phys. **175**(2), 584 (2002)
54. S. B. Pope, *Turbulent Flows*, 1st Edition ed. (Cambridge University Press, 2000).
55. J. Baggett, J. Jimenez, and A. Kravchenko, Annual research briefs, 51 (1997).
56. I. Shiryanpour, N. Kasiri, The European Physical Journal Plus **134**(5), 1 (2019)
57. J. Smagorinsky, Mon. Weather Rev. **91**(3), 99 (1963)
58. M. Germano, U. Piomelli, P. Moin, W.H. Cabot, Phys. Fluids A **3**(7), 1760 (1991)
59. U. Frisch, *Turbulence: the legacy of AN Kolmogorov*. (Cambridge University Press, 1995);

60. A.N. Kolmogorov, J. Fluid Mech. **13**(1), 82 (1962)
61. J. C. Hunt, A. A. Wray, and P. Moin, (1988).
62. J.M. Wallace, H. Eckelmann, R.S. Brodkey, J. Fluid Mech. **54**(01), 39 (1972)
63. P. Saha, G. Biswas, A. Mandal, S. Sarkar, Int. J. Heat Mass Transf. **104**, 178 (2017)